

Spatially Controlled Permeability and Stiffness in Photopatterned Two-Stage Reactive Polymer Films for Enhanced CO₂ Barrier and Mechanical Toughness

Adrienne K. Blevins, Lewis M. Cox, Leiqing Hu, Jasper A. Drisko, Haiqing Lin, Christopher N. Bowman, Jason P. Killgore, and Yifu Ding*

Cite This: *Macromolecules* 2021, 54, 44–52

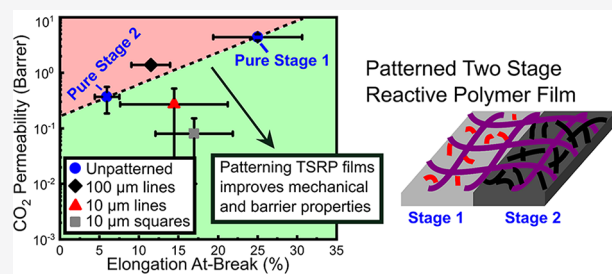
Read Online

ACCESS |

Metrics & More

Article Recommendations

ABSTRACT: Controlling the microstructure of heterogeneous, polymer membranes used in gas barrier and gas separation technologies is challenging. Being able to control composite structures is beneficial to achieve an optimum combination of gas permeation and mechanical performance. In addition, unique properties such as anisotropy and confined transport can be controlled by tailoring the size and position of constituent materials. Two-stage reactive polymer (TSRP) networks are an emerging dual-cure polymer material for spatially varying cross-linking density via photopatterning. In this work a thiol–acrylate-based TSRP was used to investigate the effects of pattern geometry on CO₂ permeability and mechanical properties. Line and square patterns of alternating high and low cross-linking density, with characteristic dimension between 1 mm and 10 μm, were generated in TSRP membranes. Notably, synergistic enhanced barrier properties were observed for 10 μm square patterns of lower cross-linking density (or higher permeability) material exhibiting two confined dimensions compared to line gratings with only one confined dimension.



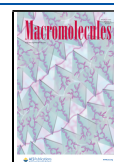
INTRODUCTION

Heterogeneous polymer-based materials are promising for commercial gas separations and gas barrier applications.^{1–3} Commonly explored examples include block copolymers (BCPs), polymer nanocomposites (PNCs), mixed matrix membranes (MMMs), and highly layered films.^{4–11} These types of materials aim to combine and maximize benefits of the components while minimizing trade-offs inherent with homogeneous materials. Performance can be enhanced beyond a simple volumetric averaging of component properties by utilizing the geometric structure of constituent materials to influence overall properties. Some advanced barrier films, for example, use inorganic platelets in a polymer matrix which retains the flexibility of the polymer while decreasing overall gas permeability. The permeability decrease results from a more tortuous diffusion pathway for penetrating molecules created by the impermeable platelet phase.¹² Advanced gas barrier materials can be found in applications ranging from food and drug packaging to encapsulation for organic electronics.^{13,14} Gases such as O₂ must be prevented from degrading the product or, often in the case of CO₂, must be kept from escaping the product. These barriers can be prepared by methods ranging from layer by layer (LBL) assembly of polymer and inorganic materials to coextruded multilayer films consisting of alternating layers of high and low permeability.^{6,15,16} Also, commonly used polymers like poly(ethylene terephthalate) and polyurethanes

can include nanomaterials dispersed by various intercalation methods.^{17,18}

The tortuous diffusion path can also be seen in MMMs for gas separations. To remove CO₂ and H₂S from natural gas, fluorinated metal–organic framework (MOF) particles are dispersed in a polymer matrix. The polymer retains processability while the MOFs are highly selective to the acid gases. Because of how the particles are distributed in the matrix, methane cannot pass through the MOFs and must travel a very tortuous path, creating a highly selective separation membrane.⁵ In addition to improving transport performance, heterogeneity can enhance the mechanical properties of polymer films. For many homogeneous polymers there is a correlation between high barrier performance and brittleness, meaning the best barriers are often excessively fragile; for ultrathin membranes, polymers with very high permeability often have undesirably low strength.^{19–21} Most applications have a general desire for

Received: October 16, 2020
 Revised: December 2, 2020
 Published: December 16, 2020



increased mechanical robustness, which is often solved by incorporating heterogeneity.^{22–24}

A major downside to heterogeneous materials, however, is that most fabrication methods have minimal control over size, position, and orientation of specific structural elements. This limits efforts to identify specific structural effects and realize theoretically predicted performance. With MMMs and PNCs, the particles can be positioned and oriented with only limited control, and at higher volume fraction they become highly susceptible to defects such as agglomeration. For BCPs and other self-assembled materials, achieving long-range order can be difficult.^{4,25} Moreover, these materials are very sensitive to component interactions and volume fractions.²⁶ Finally, for highly layered films, there exists good control over layered thickness, but geometric design freedom is limited to the vertical dimension, and interfacial voids are common. Overall, there is a need for heterogeneous polymer fabrication methods with precise control over structure.

Such a need is further emphasized by recent theoretical studies that have revealed the potential of highly controlled heterogeneous material structures for membrane applications. Restrepo-Flórez and Maldovan conducted computational fluid dynamics modeling studies on the gas separation properties of polymers with spatially controlled permeability. They observed an anisotropy effect, enabled by the precise structure control, which allowed for selectively guiding gas penetrants. Controlling the polymer properties and geometries allowed for control over the overall permeability and selectivity, and the authors were able to achieve O₂/N₂ selectivity on the order of 10³ with O₂ permeance on the order of 10⁻¹ GPU (3.35 × 10⁻¹¹ mol m⁻² s⁻¹ Pa⁻¹) and outperform the permeability versus selectivity upper bound proposed by Robeson.^{27–29}

Under these motivations, this study utilizes a two-stage reactive polymer (TSRP) network to fabricate polymer films with precisely controlled microstructure and investigate the impact of structure on gas transport and mechanical properties. A TSRP is a dual-cure polymer that is rubber after the first, base-initiated curing step (referred to here as “Stage 1”) and becomes glassy after the second, UV-initiated curing step (“Stage 2”). Features can be photopatterned in TSRPs and are only limited by the resolution of the processing technique (e.g., for a UV-initiated Stage 2, the diffraction limit) and continue to advance with improvements in additive manufacturing and photolithography technology.^{30–32} Also, unlike in multimaterial heterogeneous membranes, common defects like agglomeration or phase separation cannot occur with TSRPs, which consist of one continuous polymer network. Previous work with this TSRP patterned spatial heterogeneity at length scales down to 5 μm and demonstrated spatially varying mechanical properties, mechanical anisotropy, and a toughening effect beyond rule-of-mixtures predictions when nacre-like patterns were used.³³ Here, we test whether this structural-based property enhancement extends to gas permeation properties. This is done by photopatterning films with patterns ranging from 1 mm to 10 μm line gratings and 10 μm squares and measuring CO₂ permeability. The samples are then imaged using atomic force microscopy (AFM) to characterize the pattern and interface. By establishing an empirical correlation between permeability and AFM-measured modulus for bulk specimens with partial Stage 2 cure, the permeability of the patterned membranes can be predicted based on the AFM stiffness maps. Line-grating patterns are found to induce a reduction of permeability that is pattern-size dependent and well explained by the predictions

from the AFM modulus maps. In contrast, square-patterned specimens were predicted to have higher permeability than line patterns of equal volume fraction, but direct measurements of permeability reveal reduced permeability. Mechanical tests are also performed to demonstrate concomitant decreases in permeability with enhanced toughness and elongation at-break, important for improved gas barrier materials.

■ EXPERIMENTAL SECTION

Sample Preparation. All chemicals were purchased from MilliporeSigma and used as received following procedures detailed in previous work.³³ To summarize, a tetra-functional thiol monomer, pentaerythritol tetrakis(3-mercaptopropionate), was mixed with a trifunctional acrylate monomer, trimethylolpropane triacrylate, in a 1:2 functional group ratio.³⁴ Photoinitiator (2,2-dimethoxy-2-phenylacetophenone, 1 wt %) and inhibitor (butylated hydroxytoluene, 0.5 wt %) were added for use in the photopatterning step. Finally, trimethylamine (TEA, 0.5 wt %) was added to initiate the thiol-Michael addition reaction between thiol and acrylate groups. The resin was then mixed, degassed, and allowed to cure for 24 h at ambient conditions between hydrophobic-coated glass slides with 76.2 μm shim stock spacers on the edges. To photopattern, the resulting TSRP films were cut, coated in index-matching oil (Cargille Laboratories), and sandwiched between an etched-chrome photomask (fabricated in-house) and a UV-absorbing ND filter (Thor Laboratories). An OmniCure S2000 UV lamp with a collimating adapter was used for 180 s at 30 mW/cm² for the exposures, unless otherwise specified. Films were then rinsed in hexane to remove oil residue and dried.

After the films were photopatterned, three thickness measurements were recorded and averaged. Sample thicknesses varied between 70 and 200 μm, depending on resin viscosity at the time of casting for each batch. For thermomechanical measurements, the film was cut into 15 mm long by 3 mm wide strips. For permeability testing, the films were sandwiched between two pieces of aluminum tape with a 6.35 or 3.18 mm diameter hole, for line and square photopatterns, respectively. This aluminum support tape provided mechanical stability since thinner films were needed for an improved permeability signal. The smaller area also increased the consistency of thickness values across the test region of the sample.

Thermomechanical Properties. A DMA Q800 (TA Instruments) was used to measure thermomechanical properties of the films including glass transition temperature *T*_g, rubbery plateau modulus, elastic modulus, and elongation at-break. Temperature sweeps were run from -80 to 150 °C at 3 °C/min with uniaxial tensile oscillations at 1 Hz to measure storage modulus, loss modulus, and tan delta. The value of *T*_g was determined from the temperature of the tan delta peak. The rubbery plateau modulus *E*' was taken as an average of storage modulus between temperatures of *T*_g + 60 and 150 °C. Strain ramps were conducted at 3% strain per minute until failure. Elongation at-break was taken to be the strain at which failure occurred (results corresponding to failure outside the span region were omitted). Three replicates were measured for each sample and the values averaged.

Cross-linking density was estimated by using rubber elasticity theory.^{35–37} Bulk density (*d*) values were measured by the water displacement method and then used to calculate the molecular weight between cross-links *M*_c from

$$M_c = \frac{dR(T_g + 60)}{E'} \quad (1)$$

where *R* is the universal gas constant.

Permeation Testing. To perform gas permeability measurements, the aluminum tape-supported sample was mounted into a constant volume, variable pressure system that was built in-house. Details of this system can be found in the Supporting Information of Singh et al.³⁸ Samples were exposed to vacuum for at least 8 h to remove any residual solvents and absorbed gases, and then the cell was sealed while the pressure was recorded for at least 8 h to measure the leak rate of the system. Next, the cell was degassed and then pressurized with the test

gas to 0.21 MPa. The cell was then sealed again, and pressure was recorded for at least 8 h. Permeability P values were calculated using eq 2, where L is the thickness of the film, A is the exposed film area, Δp is the average pressure differential during the permeation test, and V_d/t and V_{dL}/t_L are the volumetric fluxes of gas that permeated through the film during the permeation test and the leak rate test, respectively.³⁹

$$P = \frac{L}{A\Delta p} \left(\frac{V_d}{t} - \frac{V_{dL}}{t_L} \right) \quad (2)$$

The permeation measurement was repeated two additional times with degassing occurring in between each, and all three values were averaged together. The samples used in this study have overall very low permeability values. CO₂ was chosen as the test gas because it gave the best signal and consistently had permeation fluxes that were higher than leak rate fluxes. It is also a commercially relevant gas to barrier and packaging applications.

Gas Sorption Testing. A gravimetric sorption analyzer of IGA 001 (Hidden Isochema, Warrington, U.K.) was used to determine the CO₂ sorption of the samples at 35 °C and varied pressures.⁴⁰ Around 70 mg of the sample was loaded and dried under a vacuum for approximately 12 h before the measurement. Gas solubility is calculated from the weight change of the sample with consideration of the buoyancy effect. The uncertainty of the gas solubility can be estimated at $\approx 10\%$ using an error propagation method.⁴⁰

AFM Characterization. After gas permeation testing, an AFM (Cypher, Asylum Research) instrument was used in fast force mapping (FFM) mode to measure the surface modulus of the polymer films. No differences were seen between films measured before and after permeation testing. A cantilever with stiffness of 5 N/m (All in One-Al, Budget Sensors) was used with an indentation force of 80 nN and fast force rate of 300 Hz. Scans were $1 \mu\text{m} \times 1 \mu\text{m}$ for unpatterned samples (i.e., pure Stage 1 and Stage 2) and $30 \mu\text{m} \times 30 \mu\text{m}$ (the maximum scan area available) for patterned samples. All pixel sizes were less than 100 nm. The FFM data were analyzed using a Hertz contact mechanics model. Due to the 300 Hz fast force rate, modulus values obtained by AFM are higher than those reported from 1 Hz DMA but do agree with DMA measurements previously taken at higher frequencies.³³

RESULTS AND DISCUSSION

The TSRP formulation used in this study is a thiol–acrylate system with an excess of acrylate groups. The first cure stage reacts all of the thiol groups with acrylate groups, and the second cure stage bonds the remaining unreacted acrylate groups, increasing cross-linking density.^{34,41,42} Figure 1A illustrates this process. TSRP films were photopatterned with 1 mm, 100 μm , and 10 μm line-space gratings as well as 10 μm masked squares. Figure 1B shows the resulting AFM FFM scans along with pure Stage 1 and pure Stage 2 scans. FFM scans reveal the resulting patterned heterogeneity in stiffness and, correspondingly, cross-linking density.

Regions that are covered by the photomask and not exposed to UV light remain soft, with modulus in the 10 MPa range, similar to pure Stage 1. This is most clearly seen in 1 mm and 100 μm line patterns. Regions exposed to UV light increased in stiffness to pure Stage 2 values, about 600 MPa. Importantly, the interfacial profile between the two stages is dependent on feature size.³³ Larger features (i.e., 1 mm and 100 μm lines) have sharp interfaces that are 13 and 6.5 μm in length (1.3% and 6.5% of total pattern length), respectively. Small differences in interface shape are likely due to differences in UV light collimation and alignment. In contrast, for patterns with feature size of 10 μm , interfaces are much broader and masked regions are partially cured due to increased amounts of light scattering and free radical diffusion. For the 10 μm patterns, pure Stage 1 values are never achieved. Instead, the unexposed regions display stiffness

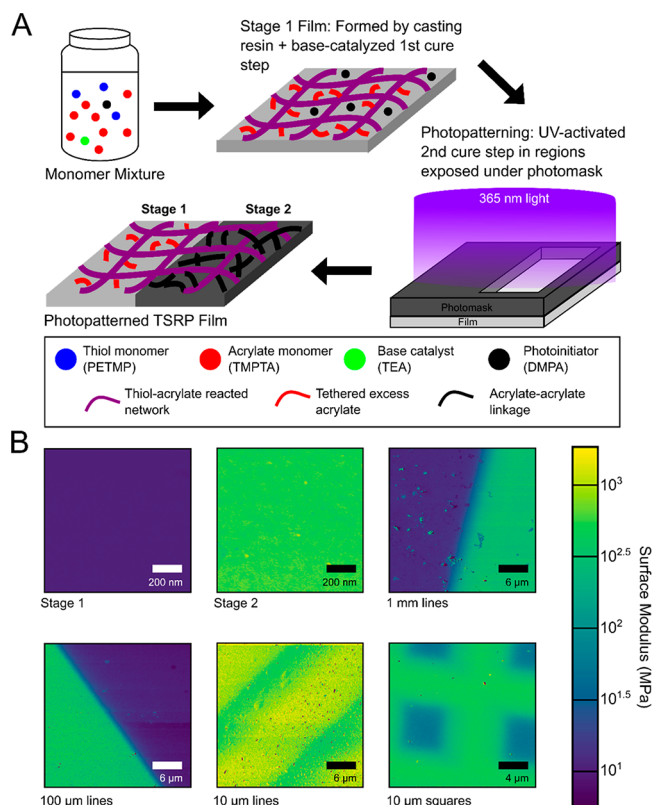


Figure 1. (A) Fabrication of patterned TSRP films with chemical component details. (B) Microscale maps of the surface modulus of patterned samples determined by AFM fast force mapping. Pure Stages 1 and 2 are also shown for comparison. All scans share the same data scale presented.

values of 170 and 50 MPa for line patterns and square patterns, respectively. Optical alignment effects are more pronounced with smaller features as well, further broadening the interface.

CO₂ permeability measurements were conducted for all samples, and the results are summarized in Figure 2, where points represent patterned sample values while solid lines indicate pure Stages 1 and 2. As expected from general trends discussed earlier, the lower-stiffness Stage 1 material has a higher permeability than the stiffer Stage 2 polymer. For patterned

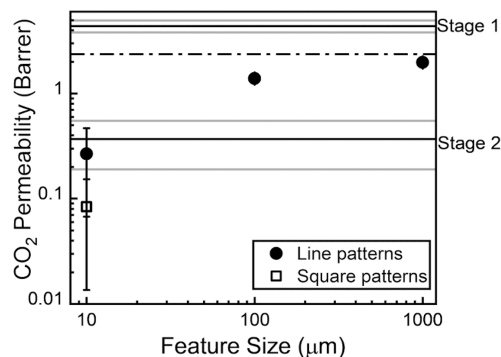


Figure 2. CO₂ permeability as a function of pattern feature size. Solid lines represent pure Stage 1 and 2 permeability values, with gray bars representing the error range. The dashed line represents the average value expected from a 50/50 vol % mixture. Vertical error bars are present on all data points, but some are smaller than the size of the symbols. One Barrer = $3.35 \times 10^{-16} \text{ mol m}^{-1} \text{ s}^{-1} \text{ Pa}^{-1}$.

samples, permeability decreases with pattern size, and the square pattern is decreased further from the line pattern of the same feature size. For all photomasks used to pattern the samples, the area fraction of masked regions is equal to the area fraction of exposed regions; this corresponds to an expected overall 0.5 volume fraction of Stage 1 and 0.5 volume fraction of Stage 2, as the patterns are assumed to transfer straight through the film based on previous work and the fact that significant differences were not seen between the front and back of AFM samples.³³ Based on a volume fraction (ϕ) averaged composite model, calculated from $P = \phi_1 P_1 + \phi_2 P_2$, the permeability of these patterns is expected to be about 2.37 Barrer, indicated as a dashed line in Figure 2.

The measured permeability values of these patterned samples increasingly deviate from the predicted average with decreased pattern size. This trend correlates with the AFM measurements: smaller features have increased levels of curing in the masked regions, leading to higher average cross-linking densities and lower average permeability values. Therefore, AFM scans reveal the decreased permeability with decreased pattern feature size to be well explained by imperfect photopattern transfer for line patterns. For the 10 μm squares, however, masked regions are less stiff than the masked regions in the 10 μm line sample, which would lead to a higher overall permeability. This is opposite from the measured values, where the square pattern had a 78% permeability decrease from the line pattern.

A structure-induced decrease in permeability has been seen both experimentally and through models. Early studies of diblock copolymers showed a difference in diffusion coefficient between small-scale morphologies.^{43,44} Layered films have also seen this with decreasing layer thickness due to confinement-induced chain alignment.¹⁵ A confined random walk diffusion simulation that incorporated cage size and cage-hopping probability values showed that confinement does slow diffusion, and results matched up well with more intensive molecular dynamics studies of real transport phenomena.⁴⁵ Random walk diffusion simulations carried out by Shen et al. where boundaries were completely confined showed that the diffusion coefficient is reduced to 67% and 33% when confined to lamellae and cylinder morphologies, respectively.⁴⁶

Diffusion-based studies, rather than permeability, are relevant to the TSRP material used in this paper because highly cross-linked sample permeability is primarily diffusion controlled, and the chemical similarities between Stage 1 and Stage 2 likely make the effect of solubility differences between the two stages small.⁴⁷ This is confirmed by CO_2 sorption measurements taken at 35 $^\circ\text{C}$. The solubility coefficients were measured to be $1.1 \pm 0.1 \text{ cm}^3(\text{STP})/\text{cm}^3 \text{ atm}$ and $0.9 \pm 0.09 \text{ cm}^3(\text{STP})/\text{cm}^3 \text{ atm}$ for Stage 1 and Stage 2 materials, respectively. These studies show that a structural-induced permeation decrease in highly controlled polymer geometries could be caused by changing properties of constituent polymers or the presence of interfaces altering gas molecule trajectories. Also, these studies have looked at smaller length scales than those investigated in this paper, and a more pronounced permeability decrease could potentially be seen by characterizing the permeability of membranes with smaller feature sizes in future work.

To determine if a structural effect is impacting overall permeability of square patterns, better predictions based on spatial averages using actual permeability of each phase are needed. To enable that, the permeability of partially cured masked regions needs to be understood. To do this, a set of four partially cured samples, A–D, was created. Curing parameters

and the resulting thermomechanical properties are detailed in Table 1 and Figure 3. Increasing the UV dose resulted in an

Table 1. Stage 1, 2, and Partially Cured Samples: UV-Curing Parameters and Glass Transition Temperature

film	cure intensity (mW/cm ²)	cure time (s)	total UV dose (J/cm ²)	T_g ($^\circ\text{C}$)
stage 1	0	0	0.00	−10.5
partial cure A	5	10	0.05	−5.9
partial cure B	5	30	0.15	7.4
partial cure C	5	180	0.45	17.4
partial cure D	15	180	2.70	32.9
stage 2	30	180	5.40	42.9

increase in T_g , as can be seen in Figure 3A. In addition, the shape of the $\tan \delta$ curves (inset) reflects the increased degree of curing. In alignment with other thiol–ene network behavior, the Stage 1 curve is a very sharp peak due to the homogeneity of the thiol–ene network.⁴⁸ As the degree of partial curing increases, the $\tan \delta$ peak gets broader, representing the increased heterogeneity of the network as more free radical acrylate–acrylate linkages are created. As confirmation of degree of curing, molecular weight between cross-links, M_c , decreases with higher UV dose as well, as shown in Figure 3B.

Surface modulus and CO_2 permeability are both measured for partially cured samples and plotted in Figures 3C and D, respectively. As seen in the modulus maps earlier, stiffer moduli correspond to higher cross-linking densities (lower M_c). The relationship between CO_2 permeability and M_c can be compared to the large set of gas permeation data for various thiol–ene polymers that Kwisnek and co-workers generated.⁴⁷ Kwisnek et al. found that cross-linked thiol–ene-based films decreased in permeability with increasing cross-linking density due to the decrease in available free volume; the films in this study follow the same trend, further indicating that the effects of excess unreacted acrylate groups in Stage 1 and partially cured samples are not significantly impacting permeability.⁴⁹ Because of the second-stage acrylate linkages, higher functionality of the monomers, and lack of CO_2 -philic groups, the films used in this study are much less permeable than those previously measured by Kwisnek and co-workers. This result shows that the cross-linking density versus permeability relationship that Kwisnek and co-workers found for thiol–ene networks still holds into the glassy regime and when a significant portion of the network has a heterogeneous structure. Other studies have found inconclusive results on the effect of cross-linking density on permeability, often due to large chemical and structural differences between networks with changing cross-linking density.⁵⁰ The results found in this study indicate that network heterogeneity and chemical group differences (e.g., reacted versus unreacted acrylate groups, unreacted photoinitiator) present in these TSRP materials are not sufficient to alter the permeation behavior from the expected trend that increased cross-linking density correlates with decreased free volume, which in turn corresponds to decreased permeability. Furthermore, this demonstrates the effectiveness of TSRP materials to use cross-linking density, instead of chemical composition, as a means to tune permeability.

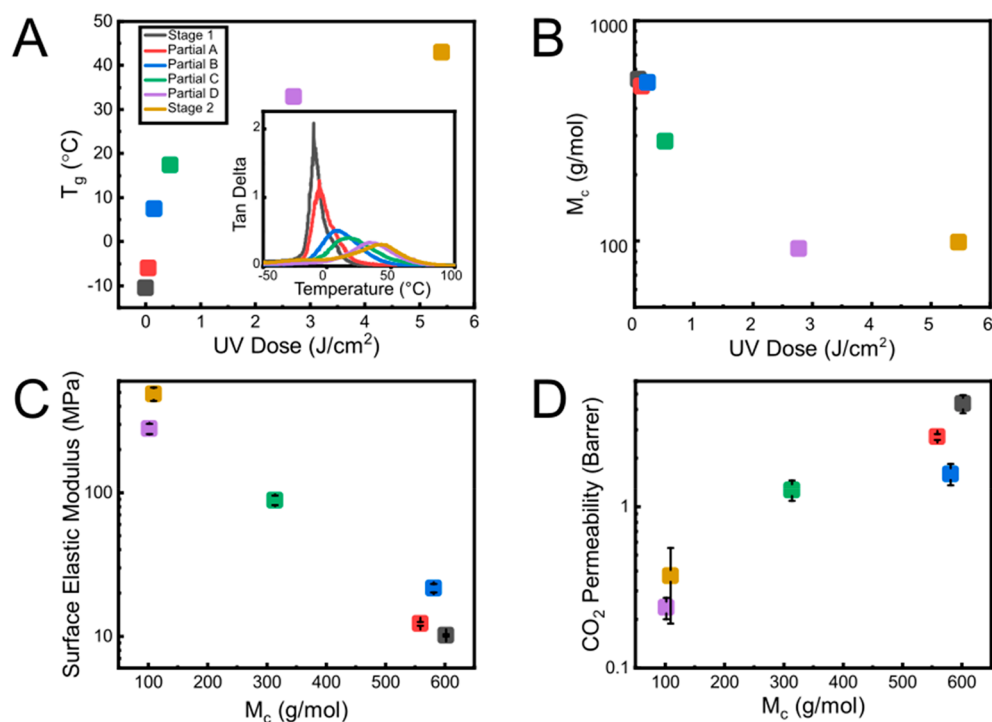


Figure 3. Partially cured, unpatterned sample properties: (A) T_g as a function of UV dose. Inset: Tan δ curves from DMA temperature scans where the T_g value is taken as the peak of the curve. (B) M_c (estimated from the rubbery plateau modulus and bulk density values) as a function of UV dose. (C) AFM-generated surface modulus (averaged from a $1 \mu\text{m} \times 1 \mu\text{m}$ scan) as a function of M_c . (D) CO_2 permeability as a function of M_c . All points in (C) and (D) have y error but may be smaller than the data point symbols. One Barrer = $3.35 \times 10^{-16} \text{ mol m}^{-1} \text{ s}^{-1} \text{ Pa}^{-1}$. All graphs share the same color legend as (A).

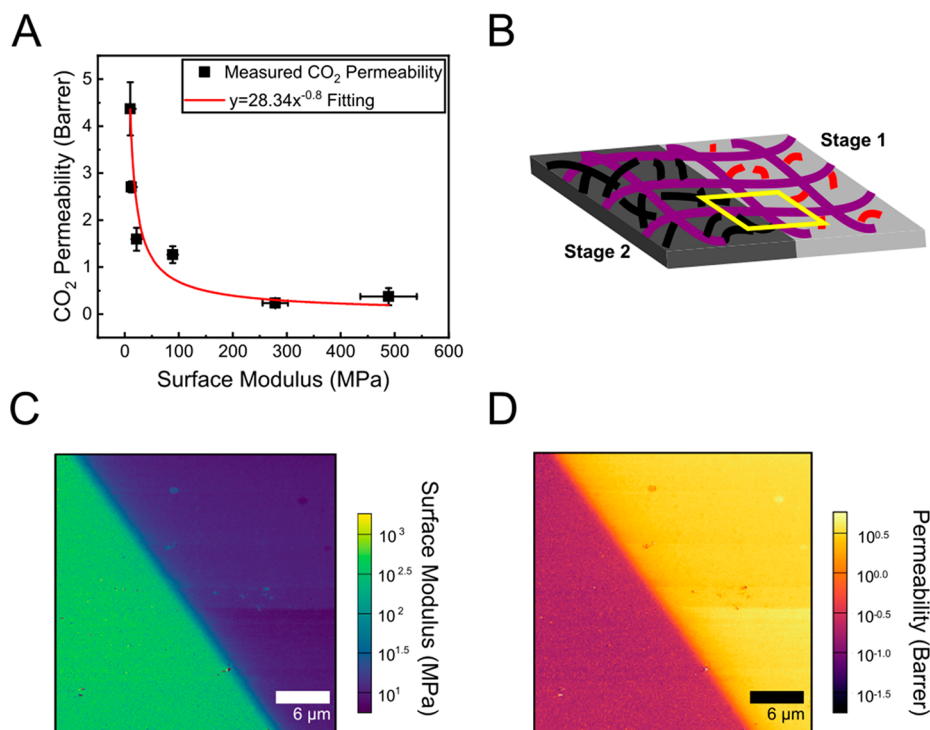


Figure 4. (A) CO_2 permeability as a function of AFM-generated surface elastic modulus. x and y errors are present for all points. The red line is the fitting equation generated by Origin. (B) Schematic of a line-patterned sample with the yellow box indicating where an AFM scan would be taken across the interface. (C) $100 \mu\text{m}$ line patterned film surface modulus map measured by AFM in FFM mode. (D) Permeation map generated by applying eq 3 to all points in (C). One Barrer = $3.35 \times 10^{-16} \text{ mol m}^{-1} \text{ s}^{-1} \text{ Pa}^{-1}$.

By incorporating the monotonic relationship between surface modulus and permeability for the varying degrees of cure in

Figure 3, modulus maps from Figure 1 can be converted into permeability maps, allowing direct comparison of pattern size

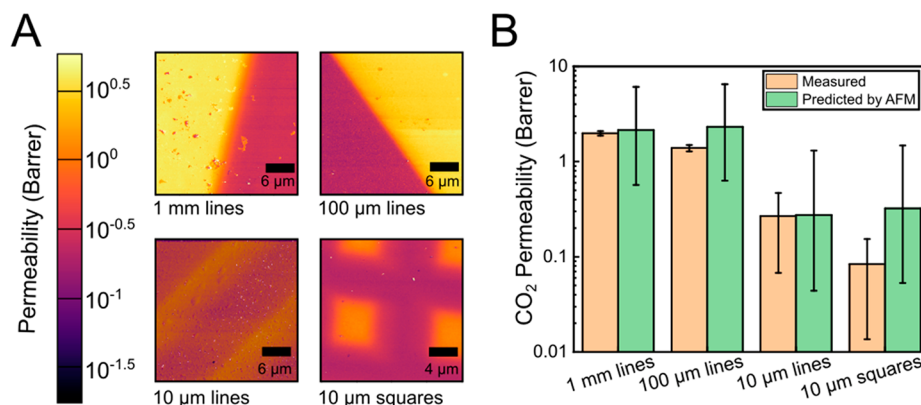


Figure 5. (A) Permeability maps for all patterned samples. All scans share the same data scale presented. Red dots in scans indicate outliers that were removed. (B) Measured CO_2 permeability as compared to the permeability predicted by averaging over AFM-generated permeability maps. One Barrer = $3.35 \times 10^{-16} \text{ mol m}^{-1} \text{ s}^{-1} \text{ Pa}^{-1}$.

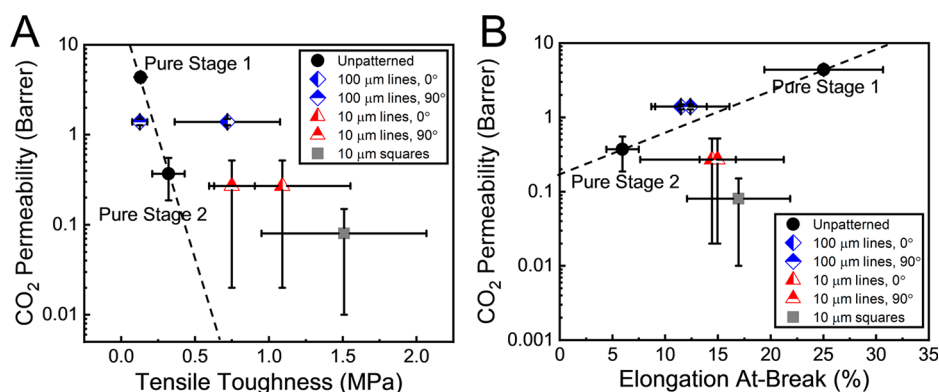


Figure 6. (A) Permeability as a function of patterned film toughness. (B) Permeability as a function of patterned film elongation at-break. Pure Stage 1 and 2 values are also included, with a dashed line indicating the trade-off present for homogeneous, unpatterned polymers. One Barrer = $3.35 \times 10^{-16} \text{ mol m}^{-1} \text{ s}^{-1} \text{ Pa}^{-1}$.

and shape effects while controlling for feature-size-dependent conversion. Permeability and surface modulus are plotted against each other in Figure 4A, along with a power law fit, with larger permeability values being more heavily weighted to allow for better matching predicted Stage 1 permeability with measured Stage 1 permeability. The resulting equation of fit is given as eq 3, where P is the permeability and E is the surface elastic modulus.

$$P = (28.34 \pm 14)E^{-0.8 \pm 0.2} \quad (3)$$

The $100 \mu\text{m}$ line patterned film is used as an example in Figure 4B–D, illustrating the permeation map conversion process. The model accurately predicts high permeability for the soft, Stage 1 region and low permeability for the stiff, Stage 2 region. Spatial averages of Stage 1 and 2 permeability maps give predicted values of 4.33 and 0.19 Barrer, respectively, which are within the standard deviation of the measured values of 4.37 ± 0.57 and 0.37 ± 0.18 Barrer. Because each scan could only capture $30 \mu\text{m}$ of the patterned samples, spatial averages of each region (Stage 1, interface, and Stage 2) were taken and weighted according to the pattern volume fraction to calculate the overall spatially averaged predicted permeability. Using AFM data is a novel method to predict spatially varying permeability from local mechanical properties. Note that the T_g value (Figure 3A) also directly correlates with the cross-link density of the films, which allows for prediction of permeability through high-resolution T_g measurements of patterned TSRP films. However, high-

resolution T_g measurement using techniques such as the nanothermal analysis (nano-TA) has a lower spatial resolution than the AFM FFM method used here, and it is often challenging to characterize highly cross-linked films.^{51,52}

After each of the modulus maps from Figure 1 are converted to permeability maps, which are shown in Figure 5A, and the result is scaled to incorporate the periodic nature of the patterns, the AFM-predicted CO_2 permeability values are compared to the measured CO_2 permeability in Figure 5B. For all line patterns, predicted values match well with measured values, confirming that imperfect photomask transfer (or increased curing in the unexposed regions) is responsible for the decrease in permeability with decreasing feature size. The $10 \mu\text{m}$ square pattern, however, is about $4\times$ lower than the AFM-predicted value. Converting from modulus to permeability for the predicted values introduces large error bars, which leads to no samples being statistically significantly different (future work will focus on lowering the error caused by low overall permeability values). A $4\times$ decrease, though, is much larger than any of the other differences seen. Square patterns, instead of lines, increase the number of confined dimensions from 1 to 2. This mimics the study conducted by Shen and co-workers, discussed earlier, which found a large decrease in diffusion coefficient from modeling lamellae to cylinder morphologies due to the increase in confined dimensions.⁴⁶ The results found here provide evidence in support of a confinement effect occurring when the more permeable phase (partially cured Stage

1 regions here) is constrained into 2D patterns at length scales on the order of 10 μm in a film with thickness on the order of 100 μm . Photocontrollable, spatially varying permeability in TSRPs can cause a structure-influenced decrease in permeability, which is a valuable materials system strategy for gas barrier applications.

To further explore the suitability of patterned TSRPs for gas barrier applications, which require low permeability and mechanical robustness, mechanical properties of these films were explored. As discussed earlier, patterned TSRP films can have improved mechanical properties due to the presence of strong interfaces, and as such it was hypothesized that these films would have an improved mechanical response with smaller, 2D patterns.³³ Accordingly, tensile toughness and elongation at-break were measured and compared for Stage 1, Stage 2, and patterned samples. One millimeter samples were not included because that length scale demonstrated no barrier improvement here or toughness enhancement in previous work. Line-spacing samples were measured parallel (0°) and perpendicular (90°) to the direction of loading to elucidate any anisotropy effects.

Figures 6A and 6B show CO_2 permeability plotted against toughness and elongation at-break, respectively. Stage 1 and 2 are representative of typical homogeneous polymers. In the context of packaging applications, Stage 1 polymer has high elongation (desirable), high permeability (undesirable), and low toughness (undesirable), while Stage 2 polymer shows low elongation (undesirable), low permeability (desirable), and low toughness (undesirable, even though slightly higher than Stage 1). The performance of partially cured samples can be interpolated by this trend.⁴⁹

Patterning with 100 μm lines results in a membrane that does not significantly deviate from this interpolated permeation versus elongation trade-off when tested at 90° , and performance falls between the pure Stage 1 and 2 values due to the presence of an interface (Figure 6B). The 90° sample toughness is comparable to the Stage 1 toughness because fracture occurs purely within the softer and weaker Stage 1 domains. However, the toughness of the 100 μm line patterned sample is evidently anisotropic. For the 0° oriented sample, the toughness is increased sixfold, from 0.12 to 0.72, because of local variations in crack driving force that can arrest the crack and increase toughness.^{53,54}

Upon reaching 10 μm line patterns, a deviation is seen from the interpolated permeation versus elongation trade-off, where permeability drops lower and elongation is approximately tripled compared to pure Stage 2 (Figure 6B). Toughness values are also increased as crack energy dissipation mechanisms are present. Anisotropy is still evident, with the same trends as the 100 μm films, but to a lesser degree because Stage 1 regions in the 10 μm patterned samples are partially cured (Figure 1).

Interestingly, the 10 μm square pattern shows an even higher increase in elongation at-break at 17% and the largest tensile toughness at 1.5 MPa (a 5 \times improvement from pure Stages 1 and 2), while still maintaining low permeability. Such an enhancement in toughness is attributed to more effective crack arresting by the 2D patterned interfaces compared with the line patterns oriented at 0° . Overall, the results demonstrate that a structure-induced effect is improving mechanical properties for these films, without the trade-off of higher permeability and, in some cases, even alongside further decreased permeability.

CONCLUSION

In this study, a TSRP network was employed to generate polymer films with spatially varying cross-link density patterned on the scale of millimeters down to micrometers. It was shown that variations in cross-linking density, and therefore mechanical properties, correlated directly to a variation in gas permeability. The patterned films, with spatial variations in gas permeability, showed a decrease in overall permeability with a decrease in pattern size and increase in pattern dimension, despite constant nominal volume fraction of both stages. A series of partially cured films were then used to develop a relationship between AFM-measured surface modulus and CO_2 permeability, which allowed for predicting a spatially averaged permeability value from AFM-generated modulus maps of patterned samples. Comparing measured to predicted values showed that most of the decrease in permeability came from imperfect photomask pattern transfer. The 10 μm square pattern, however, provided evidence that suggests a structural confinement effect impacts the gas permeability of the polymer film. Mechanical properties were also investigated to evaluate this material strategy for barrier film applications. Tensile toughness and elongation at-break both increased following the same trend as permeability decrease with the patterns. TSRPs and this patterning methodology provide many advantages, including facile and green fabrication, a high degree of pattern control, and strong interfaces. TSRPs can also be applied to many different chemistries to target specific, application-relevant properties. Overall, combining the barrier improvements with increased mechanical robustness for small patterns of soft, Stage 1 in a stiff, Stage 2 matrix shows a promising, highly controllable fabrication strategy for gas barrier applications using TSRPs.

AUTHOR INFORMATION

Corresponding Author

Yifu Ding – *Materials Science and Engineering Program and Paul M. Rady Department of Mechanical Engineering, University of Colorado, Boulder, Colorado 80303, United States*; orcid.org/0000-0001-7779-7781; Email: yifu.ding@colorado.edu

Authors

Adrienne K. Blevins – *Materials Science and Engineering Program, University of Colorado, Boulder, Colorado 80303, United States*

Lewis M. Cox – *Mechanical and Industrial Engineering Department, Montana State University, Bozeman, Montana 59715, United States*

Leiying Hu – *Department of Chemical and Biological Engineering, University at Buffalo, The State University of New York, Buffalo, New York 14260, United States*

Jasper A. Drisko – *Radio Frequency Technology Division, National Institute of Standards and Technology, Boulder, Colorado 80305, United States*

Haiqing Lin – *Department of Chemical and Biological Engineering, University at Buffalo, The State University of New York, Buffalo, New York 14260, United States*; orcid.org/0000-0001-8042-154X

Christopher N. Bowman – *Materials Science and Engineering Program and Department of Chemical and Biological Engineering, University of Colorado, Boulder, Colorado 80303, United States*; orcid.org/0000-0001-8458-7723

Jason P. Killgore – Applied Chemicals and Materials Division, National Institute of Standards and Technology, Boulder, Colorado 80305, United States

Complete contact information is available at:

<https://pubs.acs.org/10.1021/acs.macromol.0c02355>

Author Contributions

The manuscript was written through contributions of all authors. All authors have given approval to the final version of the manuscript.

Notes

The authors declare no competing financial interest.

ACKNOWLEDGMENTS

The authors gratefully acknowledge research support from the National Science Foundation (NSF) Industry/University Cooperative Research Center for Membrane Science, Engineering and Technology (MAST) at the University of Colorado Boulder (UCB, award number, IIP 1624602). Acknowledgment is made to the Donors of the American Chemical Society Petroleum Research Fund for partial support of this research. The authors gratefully acknowledge Collin Dunn in Dr. Doug Gin's lab at CU Boulder for access to and assistance with the gas permeation experiments. Certain commercial equipment, instruments, or materials are identified in this paper in order to specify the experimental procedure adequately. Such identification is not intended to imply recommendation or endorsement by NIST. Contribution of NIST, an agency of the U.S. government; not subject to copyright.

REFERENCES

- (1) Koros, W. J.; Zhang, C. Materials for Next-Generation Molecularly Selective Synthetic Membranes. *Nat. Mater.* **2017**, *16* (3), 289–297.
- (2) Baker, R. W.; Low, B. T. Gas Separation Membrane Materials: A Perspective. *Macromolecules* **2014**, *47* (20), 6999–7013.
- (3) Dhoot, S. N.; Freeman, B. D.; Stewart, M. E. Barrier Polymers. *Encycl. Polym. Sci. Technol.* **2002**, DOI: 10.1002/0471440264.pst025.
- (4) Nunes, S. P.; Car, A. From Charge-Mosaic to Micelle Self-Assembly: Block Copolymer Membranes in the Last 40 Years. *Ind. Eng. Chem. Res.* **2013**, *52* (3), 993–1003.
- (5) Kalaj, M.; Bentz, K. C.; Ayala, S.; Palomba, J. M.; Barcus, K. S.; Katayama, Y.; Cohen, S. M. MOF-Polymer Hybrid Materials: From Simple Composites to Tailored Architectures. *Chem. Rev.* **2020**, *120*, 8267–8302.
- (6) Priolo, M. A.; Holder, K. M.; Guin, T.; Grunlan, J. C. Recent Advances in Gas Barrier Thin Films via Layer-by-Layer Assembly of Polymers and Platelets. *Macromol. Rapid Commun.* **2015**, *36* (10), 866–879.
- (7) Pethe, V. V.; Wang, H. P.; Hiltner, A.; Baer, E.; Freeman, B. D. Oxygen and Carbon Dioxide Permeability of EAA/PEO Blends and Microlayers. *J. Appl. Polym. Sci.* **2008**, *110* (3), 1411–1419.
- (8) Galizia, M.; Chi, W. S.; Smith, Z. P.; Merkel, T. C.; Baker, R. W.; Freeman, B. D. 50th Anniversary Perspective: Polymers and Mixed Matrix Membranes for Gas and Vapor Separation: A Review and Prospective Opportunities. *Macromolecules* **2017**, *50* (20), 7809–7843.
- (9) Buonomenna, M. G.; Yave, W.; Golemme, G. Some Approaches for High Performance Polymer Based Membranes for Gas Separation: Block Copolymers, Carbon Molecular Sieves and Mixed Matrix Membranes. *RSC Adv.* **2012**, *2* (29), 10745.
- (10) Cui, Y.; Kundalwal, S. I.; Kumar, S. Gas Barrier Performance of Graphene/Polymer Nanocomposites. *Carbon* **2016**, *98*, 313–333.
- (11) Mondal, S. Review on Nanocellulose Polymer Nanocomposites. *Polym.-Plast. Technol. Eng.* **2018**, *57* (13), 1377–1391.
- (12) Cui, Y.; Kumar, S.; Rao Kona, B.; van Houcke, D. Gas Barrier Properties of Polymer/Clay Nanocomposites. *RSC Adv.* **2015**, *5* (78), 63669–63690.
- (13) Arora, A.; Padua, G. W. Review: Nanocomposites in Food Packaging. *J. Food Sci.* **2010**, *75* (1), R43–R49.
- (14) Logothetidis, S.; Laskarakis, A.; Georgiou, D.; Amberg-Schwab, S.; Weber, U.; Noller, K.; Schmidt, M.; Küçükpinar-Niarchos, E.; Lohwasser, W. Ultra High Barrier Materials for Encapsulation of Flexible Organic Electronics. *Eur. Phys. J.: Appl. Phys.* **2010**, *51* (3), 33203.
- (15) Wang, H.; Keum, J. K.; Hiltner, A.; Baer, E.; Freeman, B.; Rozanski, A.; Galeski, A. Confined Crystallization of Polyethylene Oxide in Nanolayer Assemblies. *Science* **2009**, *323* (5915), 757–760.
- (16) Li, Z.; Olah, A.; Baer, E. Micro- and Nano-Layered Processing of New Polymeric Systems. *Prog. Polym. Sci.* **2020**, *102*, 101210.
- (17) Ke, Z.; Yongping, B. Improve the Gas Barrier Property of PET Film with Montmorillonite by in Situ Interlayer Polymerization. *Mater. Lett.* **2005**, *59* (27), 3348–3351.
- (18) Joshi, M.; Adak, B.; Butola, B. S. Polyurethane Nanocomposite Based Gas Barrier Films, Membranes and Coatings: A Review on Synthesis, Characterization and Potential Applications. *Prog. Mater. Sci.* **2018**, *97*, 230–282.
- (19) Sangroniz, A.; Zhu, J.-B.; Tang, X.; Etxeberria, A.; Chen, E. Y.-X.; Sardon, H. Packaging Materials with Desired Mechanical and Barrier Properties and Full Chemical Recyclability. *Nat. Commun.* **2019**, *10* (1), 3559.
- (20) Lagaron, J. M.; Catalá, R.; Gavara, R. Structural Characteristics Defining High Barrier Properties in Polymeric Materials. *Mater. Sci. Technol.* **2004**, *20* (1), 1–7.
- (21) Pournaghshband Isfahani, A.; Sadeghi, M.; Wakimoto, K.; Shrestha, B. B.; Bagheri, R.; Sivaniah, E.; Ghalei, B. Pentiptycene-Based Polyurethane with Enhanced Mechanical Properties and CO₂-Plasticization Resistance for Thin Film Gas Separation Membranes. *ACS Appl. Mater. Interfaces* **2018**, *10* (20), 17366–17374.
- (22) Humood, M.; Chowdhury, S.; Song, Y.; Tzeng, P.; Grunlan, J. C.; Polycarpou, A. A. Nanomechanical Behavior of High Gas Barrier Multilayer Thin Films. *ACS Appl. Mater. Interfaces* **2016**, *8* (17), 11128–11138.
- (23) Im, H.-G.; Park, H. Y.; Kang, D. J. Class-II-Type Nanosilica-Epoxy Hybrid Coating with High Moisture Barrier Performance and Mechanical Robustness. *Prog. Org. Coat.* **2019**, *126*, 136–141.
- (24) Miller, D. C.; Foster, R. R.; Zhang, Y.; Jen, S.-H.; Bertrand, J. A.; Lu, Z.; Seghete, D.; O'Patchen, J. L.; Yang, R.; Lee, Y.-C.; George, S. M.; Dunn, M. L. The Mechanical Robustness of Atomic-Layer- and Molecular-Layer-Deposited Coatings on Polymer Substrates. *J. Appl. Phys.* **2009**, *105* (9), No. 093527.
- (25) Majewski, P. W.; Yager, K. G. Rapid Ordering of Block Copolymer Thin Films. *J. Phys.: Condens. Matter* **2016**, *28* (40), 403002.
- (26) Wolf, C.; Angellier-Coussy, H.; Gontard, N.; Doghieri, F.; Guillard, V. How the Shape of Fillers Affects the Barrier Properties of Polymer/Non-Porous Particles Nanocomposites: A Review. *J. Membr. Sci.* **2018**, *556*, 393–418.
- (27) Robeson, L. M. The Upper Bound Revisited. *J. Membr. Sci.* **2008**, *320* (1–2), 390–400.
- (28) Restrepo-Flórez, J.-M.; Maldovan, M. Breaking Separation Limits in Membrane Technology. *J. Membr. Sci.* **2018**, *566*, 301–306.
- (29) Restrepo-Flórez, J. M.; Maldovan, M. Mass Separation by Metamaterials. *Sci. Rep.* **2016**, *6* (1), 21971.
- (30) Zhang, X.; Xi, W.; Huang, S.; Long, K.; Bowman, C. N. Wavelength-Selective Sequential Polymer Network Formation Controlled with a Two-Color Responsive Initiation System. *Macromolecules* **2017**, *50* (15), 5652–5660.
- (31) Alim, M. D.; Glugla, D. J.; Mavila, S.; Wang, C.; Nystrom, P. D.; Sullivan, A. C.; McLeod, R. R.; Bowman, C. N. High Dynamic Range (Δn) Two-Stage Photopolymers via Enhanced Solubility of a High Refractive Index Acrylate Writing Monomer. *ACS Appl. Mater. Interfaces* **2018**, *10* (1), 1217–1224.

(32) Berg, G. J.; Gong, T.; Fenoli, C. R.; Bowman, C. N. A Dual-Cure, Solid-State Photoresist Combining a Thermoreversible Diels–Alder Network and a Chain Growth Acrylate Network. *Macromolecules* **2014**, *47* (10), 3473–3482.

(33) Cox, L. M.; Blevins, A. K.; Drisko, J. A.; Qi, Y.; Ding, Y.; Fiedler-Higgins, C. I.; Long, R.; Bowman, C. N.; Killgore, J. P. Tunable Mechanical Anisotropy, Crack Guiding, and Toughness Enhancement in Two-Stage Reactive Polymer Networks. *Adv. Eng. Mater.* **2019**, *21* (8), 1900578.

(34) Nair, D. P.; Cramer, N. B.; Gaipa, J. C.; McBride, M. K.; Matherly, E. M.; McLeod, R. R.; Shandas, R.; Bowman, C. N. Two-Stage Reactive Polymer Network Forming Systems. *Adv. Funct. Mater.* **2012**, *22* (7), 1502–1510.

(35) Hill, L. W. Dynamic Mechanical Properties of Polymers. In *Applied Polymer Science: 21st Century*; Craver, C. D., Carraher, C. E., Jr., Eds.; Elsevier: Amsterdam, Netherlands, 2000; pp 913–926.

(36) Cole, M. A.; Bowman, C. N. Synthesis and Characterization of Thiol-Ene Functionalized Siloxanes and Evaluation of Their Cross-linked Network Properties. *J. Polym. Sci., Part A: Polym. Chem.* **2012**, *50* (20), 4325–4333.

(37) Fairbanks, B. D.; Scott, T. F.; Kloxin, C. J.; Anseth, K. S.; Bowman, C. N. Thiol–Yne Photopolymerizations: Novel Mechanism, Kinetics, and Step-Growth Formation of Highly Cross-Linked Networks. *Macromolecules* **2009**, *42* (1), 211–217.

(38) Singh, Z. V.; Tan, L.-L.; Cowan, M. G.; Yang, Y.-W.; Zhang, W.; Gin, D. L.; Noble, R. D. Pillar [5]Arene/MatrimidTM Materials for High-Performance Methane Purification Membranes. *J. Membr. Sci.* **2017**, *539*, 224–228.

(39) *Polymer Permeability*; Comyn, J., Ed.; Springer Netherlands: Dordrecht, Netherlands, 1985. DOI: 10.1007/978-94-009-4858-7.

(40) Hu, L.; Liu, J.; Zhu, L.; Hou, X.; Huang, L.; Lin, H.; Cheng, J. Highly Permeable Mixed Matrix Materials Comprising ZIF-8 Nanoparticles in Rubbery Amorphous Poly(Ethylene Oxide) for CO₂ Capture. *Sep. Purif. Technol.* **2018**, *205*, 58–65.

(41) Nair, D. P.; Podgórski, M.; Chatani, S.; Gong, T.; Xi, W.; Fenoli, C. R.; Bowman, C. N. The Thiol-Michael Addition Click Reaction: A Powerful and Widely Used Tool in Materials Chemistry. *Chem. Mater.* **2014**, *26* (1), 724–744.

(42) Konuray, O.; Fernández-Francos, X.; Ramis, X.; Serra, À. State of the Art in Dual-Curing Acrylate Systems. *Polymers* **2018**, *10* (2), 178.

(43) Sax, J.; Ottino, J. M. Modeling of Transport of Small Molecules in Polymer Blends: Application of Effective Medium Theory. *Polym. Eng. Sci.* **1983**, *23* (3), 165–176.

(44) Kinning, D. J.; Thomas, E. L.; Ottino, J. M. Effect of Morphology on the Transport of Gases in Block Copolymers. *Macromolecules* **1987**, *20* (5), 1129–1133.

(45) Calvo-Muñoz, E. M.; Selvan, M. E.; Xiong, R.; Ojha, M.; Keffer, D. J.; Nicholson, D. M.; Egami, T. Applications of a General Random-Walk Theory for Confined Diffusion. *Phys. Rev. E* **2011**, *83* (1), No. 011120.

(46) Shen, K.-H.; Brown, J. R.; Hall, L. M. Diffusion in Lamellae, Cylinders, and Double Gyroid Block Copolymer Nanostructures. *ACS Macro Lett.* **2018**, *7* (9), 1092–1098.

(47) Kwisnek, L. Photopolymerized Thiol–Ene Networks for Gas Barrier and Membrane Applications. Ph.D. Thesis, The University of Southern Mississippi, Hattiesburg, MS, 2011.

(48) Hoyle, C. E.; Bowman, C. N. Thiol-Ene Click Chemistry. *Angew. Chem., Int. Ed.* **2010**, *49* (9), 1540–1573.

(49) Kwisnek, L.; Goetz, J.; Meyers, K. P.; Heinz, S. R.; Wiggins, J. S.; Nazarenko, S. PEG Containing Thiol–Ene Network Membranes for CO₂ Separation: Effect of Cross-Linking on Thermal, Mechanical, and Gas Transport Properties. *Macromolecules* **2014**, *47* (10), 3243–3253.

(50) Lin, H.; Kai, T.; Freeman, B. D.; Kalakkunnath, S.; Kalika, D. S. The Effect of Cross-Linking on Gas Permeability in Cross-Linked Poly(Ethylene Glycol Diacrylate). *Macromolecules* **2005**, *38* (20), 8381–8393.

(51) Maruf, S. H.; Ahn, D. U.; Pellegrino, J.; Killgore, J. P.; Greenberg, A. R.; Ding, Y. Correlation between Barrier Layer Tg and a Thin-Film

Composite Polyamide Membrane's Performance: Effect of Chlorine Treatment. *J. Membr. Sci.* **2012**, *405–406*, 167–175.

(52) Maruf, S. H.; Ahn, D. U.; Greenberg, A. R.; Ding, Y. Glass Transition Behaviors of Interfacially Polymerized Polyamide Barrier Layers on Thin Film Composite Membranes via Nano-Thermal Analysis. *Polymer* **2011**, *52* (12), 2643–2649.

(53) Kolednik, O.; Predan, J.; Fischer, F. D.; Fratzl, P. Improvements of Strength and Fracture Resistance by Spatial Material Property Variations. *Acta Mater.* **2014**, *68*, 279–294.

(54) Fratzl, P.; Gupta, H. S.; Fischer, F. D.; Kolednik, O. Hindered Crack Propagation in Materials with Periodically Varying Young's Modulus—Lessons from Biological Materials. *Adv. Mater.* **2007**, *19* (18), 2657–2661.